## S1 Background and Context for the Test Geometry

The axisymmetric body of revolution geometry used in this study and the fully appended variant (known as the BB2) have featured in a number of experimental and computational studies, see Fureby et al. (2016); Manovski et al. (2020); Lee et al. (2024) and references therein. The geometry has been adopted internationally as a benchmark geometry for validation of experimental and computational methods (Bettle, 2018; Carrica et al., 2021). These studies highlight that the key to accurate flow fields lies in the computational simulations' ability to effectively capture the near-wall flow behaviour, especially at low angles of incidence where the influence of viscous drag force is predominant. Accurate measurement of the TBL flow, turbulence levels and spectral content is therefore of high importance and a focus of this study.

In Manovski et al. (2020), a high resolution ($6600 \times 4400$ px$^2$) camera with large focal length lens (400 mm) was used to conduct long-distance, high magnification PIV, which enabled TBL measurements over the same body of revolution geometry. That study underscored the benefits of employing PIV for measuring the flow field around this geometry, notably its capability to capture the streamwise and wall-normal velocity components with high spatial resolution. Unlike traditional methods such as hot-wires or pressure probes, PIV proves to be reliable in conditions of high flow angularity and reverse flow scenarios (as supported by Willert et al., 2021), making it especially suitable for analysing flow over the tail section. In the study by Manovski et al. (2020), the TBL's mean and fluctuating velocity components were found to compare well with a Pitot probe and standard hot-wire measurements. The evolution of the boundary layer thickness and mean streamwise velocity along the streamwise direction closely conformed to a flat plate TBL in the parallel mid-body section of the geometry, where the flow is subjected to a near ZPG. A comparison of the experimental Reynolds stresses with DNS of a ZPG TBL on a flat plate indicated lower turbulence levels, which were primarily attributed to the spatial averaging present in both hot-wire and PIV measurements. To verify this, the approach of Lee et al. (2016) was adopted, thereby filtering the DNS data to match the spatial resolution of the PIV and hot-wire measurements. The comparison revealed that the measured turbulence levels were generally higher than the spatially filtered DNS data. However, definitive conclusions about the measured turbulence levels relative to the DNS could not be made due to limitations in the temporal resolution of the hot-wire, uncertainties in its active length and wire wall-normal location, and uncertainties in the laser sheet thickness. This study presents an opportunity to re-examine these TBL flows using TR-PIV and new highly resolved hot-wire measurements.

## S2 Oil Film Interferometry

Previous work on this geometry (Manovski et al., 2020, 2022) used the Clauser chart to estimate $U_\tau$, albeit with an acknowledgement of its diminished fidelity in conditions involving non-ZPG and non-equilibrium TBLs. Consequently, this study adopts the oil film interferometry (OFI) technique to measure the shear stress and friction velocity directly, leveraging its high accuracy and ability to work under pressure gradients and curvature. Örlü and Vinuesa (2020) summarise recent studies and developments in wall shear stress measurements. They highlight that, when executed precisely, OFI can achieve the lowest uncertainties in mean shear stress measurement, typically below 1.5%, compared with other test techniques. This is corroborated by Naughton and Liu (2007) and further supported by a more recent investigation by Gluzman et al. (2022), which documents an accuracy of 1–2% even under conditions of high curvature and adverse pressure gradients. The determination of wall mean shear stress via OFI relies on the thinning rate of the oil film, which is dependent on the wall shear stress, provided the oil film remains sufficiently thin, and the variation of wall shear stress across the measurement area is minimal.

This study used Xiameter$^{\text{TM}}$ PMX-200 silicon oil with nominal viscosity 100 cSt. Following, Naughton and Liu (2007), black Mylar film (40 µm thickness equivalent up to 3.5 wall units) was attached to the surface to provide a smooth reflective surface that can best capture the internal reflections required to generate the fringe pattern. A 29 Mpx camera with 200 mm lens is positioned directly above the test region, with a stand-off distance of approximately 1.4 m. This setup achieved a spatial resolution of 35 px/mm. A high-powered white LED light provided illumination. Near monochromatic light was obtained by fitting a 532 nm ± 5 nm band-pass filter to the camera lens, such that only a small narrowband of light is recorded by the camera.

A critical aspect of the OFI technique is calibrating oil viscosity to account for ambient temperature variations. Prior to conducting OFI measurements, the oil's viscosity, $\nu_o$, was calibrated using a constant temperature water bath and an Ubbelohde viscometer. This procedure enabled the derivation of an exponential relationship between temperature and viscosity, as outlined by Ng et al. (2007), ensuring the accuracy of the OFI technique under varying test conditions. The oil's temperature on the model's surface is another crucial parameter, and was measured immediately after testing by a handheld infrared thermometer (Fluke 63).

The imaging of the droplet was orthogonal to the top of the surface of the cylindrical section of the model. The oil droplet and subsequent interference fringe pattern were positioned and centred near the optical axis to minimise perspective distortions. The lens aperture was set to $f_{\#} = 4$ to minimise the depth-of-field. Due to the relatively large focal length of the objective lens (200 mm) and considerable stand-off distance (1.4 m), the impacts of perspective viewing and surface curvature were deemed negligible. This setup facilitated a linear calibration within a confined interrogation area, approximately 4 mm by 4 mm. At such a stand-off distance and viewing angle of 12.3°, the imaging rays within this small central area can be considered nearly parallel. These assumptions are validated by Naughton and Liu (2007), who show that for a stand-off distance of 2 m and local surface angle of 15°, the corresponding error in the fringe spacing is less than 0.5%.

In the tail section, the camera viewing angle remained orthogonal to the model axis of symmetry. By considering the local tail surface angle, the fringe spacing imaged by the camera was transformed to be tangent to the wall. The fringe spacing tangent to the wall ($S_w$) is given by $S_w = S_c/\cos(\theta_w)$, where $S_c$ is the fringe spacing measured by the camera and $\theta_w$ is the local wall angle.

For each OFI measurement case, an image is captured every 0.5 s with 0.35 ms exposure time for 100–200 images. The fringe spacing or period was determined using the spatial fast-Fourier-transform (FFT) method, as outlined by Ng et al. (2007). This approach identifies the fringe spacing by locating the peak Fourier mode across a row of pixels. In this study, a 3-point Gaussian peak fitting method (akin to what is used in PIV) was employed to improve the accuracy of the peak detection. Subsequently, the fringe spacing is plotted as a function of time, and the thinning rate was derived from the slope of the best-fit line, determined through least-squares linear regression. The shear stress was then determined for 40 rows of pixels, which cover a span-wise extent of 1.1 mm. These were all averaged to provide an overall mean shear stress result. The standard error of the shear stress was estimated to be ±0.7%, and represents twice the standard deviation (95% confidence interval) of the shear stress across the 40 rows of streamwise pixels. The total uncertainty in the skin friction coefficient and friction velocity is estimated to be ±1.5%.

The skin friction results are plotted in Fig. S.1, where a comparison is shown between different methods, including Clauser chart estimates from the new hot-wire data and high-resolution PIV from Manovski et al. (2020). The methods generally agree well, with the OFI results typically within 2-5% of Clauser chart estimates. There is notably more scatter between the methods in the tail section ($x/L = 0.8$ and 0.9), where the pressure gradient has a larger influence on the accuracy of the Clauser chart estimates. From here forward, the OFI skin friction results are used to obtain the friction velocity (viz. $U_\tau^2 = C_f U_e^2/2$). Preston tube measurements and Clauser chart estimates in Manovski et al. (2020) show a peak $C_f$ value near the nose, followed by a steep decrease over the bow. In the current study, measurements begin at $x/L = 0.25$, revealing a slightly elevated $C_f$ value that gradually subsides as the flow approaches the ZPG, remaining relatively constant between $x/L = 0.45$ and 0.65. At $x/L = 0.7$, a slight increase in $C_f$ is observed, which is expected due to the influence of the FPG. This location, $x/L = 0.7$, marks the transition from the cylindrical section to the tail contraction. Beyond this point, $C_f$ decreases as the APG begins to dominate.

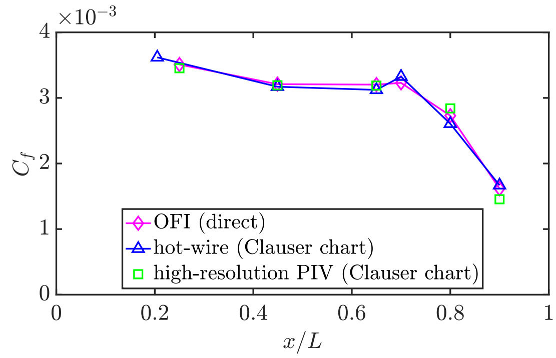


**Fig. S.1** Distribution of skin-friction coefficient ($C_f$) along model geometry as determined by different methods. High-resolution PIV are from Manovski et al. (2020). Hot-wire and OFI are from the current study. The method of determination of $C_f$ is indicated in the parenthesis.

## S3 Spatial Filtering of Direct Numerical Simulations

To obtain spatially filtered DNS data that match the spatial resolution of each measurement technique, we use the DNS snapshots from Sillero et al. (2013). A cropped streamwise extent is taken, $N_x = 1284$ grid points, from the full $N_x = 15361$ grid points of the evolving ZPG TBL. This region encompasses the Reynolds number of interest at the midpoint of the extracted section. To ensure the selected streamwise length was appropriate, the boundary layer mean and variance were assessed at the start, middle, and end of the section, showing minimal variation throughout. The DNS data were then filtered using a volumetric spatial boxcar filter to simulate the spatial resolution of the PIV and hot-wire measurements. Such a filtering technique for a DNS dataset to alter the original spatial resolution has been previously used, for example, in Chin et al. (2009); Atkinson et al. (2013). The spatial filtering process used in this study is outlined in the steps below:

1. Interpolate the data to a constant wall-normal grid spacing of 5 wall units (as the original DNS wall-normal grid is logarithmically spaced).
2. Apply a moving window spatial average in the spanwise $y$-direction without overlap, with window length equal to the effective viscous scaled laser-sheet thickness or hot-wire length. Slide the window by each span-wise grid-point. The endpoints are discarded to ensure a consistent window length.
3. Apply a moving window spatial average with 50% overlap in the $z$-direction, with a window length equal to the corresponding $IW$ size. The grid-points are centred at the middle of each window, i.e. separated by half the window length. The endpoints are again discarded to ensure a consistent window length.
4. Apply a moving window spatial average with 50% overlap in the $x$-direction, with a window length equal to the corresponding $IW$ size. The grid-points are centred at the middle of each window and are separated by half the window length. The endpoints are again discarded to ensure a consistent window length.

The constant wall-normal spacing of $5^+$ used for interpolating the DNS was chosen to ensure adequate resolution of flow features outside the inner layer ($z^+ > 50$), where velocity gradients are lower and larger scales dominate (Sillero et al., 2013). This grid was constructed isotropically without adjustments for spatial resolution of the TR-PIV out-of-plane (i.e., laser sheet thickness). The variation in laser sheet thickness over the wall-normal measurement extent of 55 mm is negligible, as supported by simple lens theory calculations, which indicate that the variations are less than 0.01 mm (equivalent to 1 wall unit).

The DNS-filtered data to match the spatial resolution of the hot-wire were obtained by applying only steps 1 and 2, with the window length equal to the viscous scaled hot-wire length ($l^+$). The resultant volumetric filtered DNS datasets are then used to obtain the statistical quantities. As an independent confirmation of the filtering process, the approach described in Lee et al. (2016) was used to filter the DNS to match the finite size of the TR-PIV and hot-wire. The comparison between the two methods confirmed that the current filtering process was consistent with the missing energy approach and the tool developed by Lee et al. (2016).

We have previously noted that iterative PIV processing with image deformation can alter the shape of $IW$s. Analysis of the deformed window shapes from the DaVis PIV software indicates they remain mostly square, suggesting that deformation effects are minimal in most regions, although $IW$s deform more near the wall due to higher velocity gradients. Accurately modelling these effects is challenging, so we have simplified the analysis by assuming a square $IW$ and neglecting variations in laser sheet thickness, which are minimal. Furthermore, we acknowledge that the rectangular (boxcar) filter used to simulate spatial averaging may not accurately represent the spatial filtering in actual hot-wire and TR-PIV measurements due to the inherent Gaussian spatial filtering effect of the measuring sensor or laser sheet. Previous studies (Samie et al., 2018) have observed non-uniform temperature profiles across hot-wires, leading to variations in sensor sensitivity along their span. In practice, the effective length sensing velocity is shorter than the sensor's physical length, meaning a boxcar filter may apply slightly more aggressive filtering than a real hot-wire. In PIV studies, the Gaussian laser beam profile results in variations in particle intensities across the laser sheet thickness. Each imaged particle's contribution to the PIV cross-correlation function within the $IW$ is weighted by its size and image intensity. As a result, we aimed at establishing an effective laser sheet thickness. For the in-plane components, the $IW$ size establishes a nominal length scale for velocity measurement in 2D TR-PIV. However, the effective resolution is also influenced by particle distribution, seeding density, and local flow gradients within the $IW$. A well-chosen $IW$ size combined with appropriate particle seeding ensures accurate velocity measurement, but the true effective length scale for in-plane components is a contribution of all three factors. Varying the particle density and distribution within the $IW$ requires a highly controlled experimental setup, which is impractical for most large-scale wind tunnel measurements, or the use of simulated particle flow fields, which is beyond the scope of this study. Therefore, we use the $IW$ size to reasonably approximate the spatial resolution for both in-plane components.

## References


C. Atkinson, N. A. Buchmann, O. Amili, and J. Soria. On the appropriate filtering of PIV measurements of turbulent shear flows. *Experiments in Fluids*, 55(1):1654, Dec 2013. ISSN 1432-1114. doi: 10.1007/s00348-013-1654-8. URL `https://doi.org/10.1007/s00348-013-1654-8`.

M. Bettle. Baseline predictions of BB2 submarine hydrodynamics for the NATO AVT-301 collaborative exercise. Technical Report DRDC-RDDC-2017-R200, Defence Research and Development Canada, 2018.

P. M. Carrica, M. Kerkvliet, F. Quadvlieg, and J. E. Martin. CFD Simulations and Experiments of a Submarine in Turn, Zigzag, and Surfacing Maneuvers. *Journal of Ship Research*, 65(04):293–308, 12 2021. ISSN 0022-4502. doi: 10.5957/JOSR.07200045. URL `https://doi.org/10.5957/JOSR.07200045`.

C. C. Chin, N. Hutchins, A. S. H. Ooi, and I. Marusic. Use of direct numerical simulation (DNS) data to investigate spatial resolution issues in measurements of wall-bounded turbulence. *Measurement Science and Technology*, 20(11):115401, sep 2009. doi: 10.1088/0957-0233/20/11/115401. URL `https://dx.doi.org/10.1088/0957-0233/20/11/115401`.

C. Fureby, B. Anderson, D. Clarke, L. Erm, S. Henbest, M. Giacobello, D. Jones, M. Nguyen, M. Johansson, M. Jones, C. Kumar, S.-K. Lee, P. Manovski, D. Norrison, K. Petterson, G. Seil, B. Woodyatt, and S. Zhu. Experimental & numerical study of a conventional submarine at $10^\circ$ yaw. *Ocean Engineering*, 116:1–20, 2016.

I. Gluzman, P. Gray, K. Mejia, T. C. Corke, and F. O. Thomas. A simplified photogrammetry procedure in oil-film interferometry for accurate skin-friction measurement over arbitrary geometries. *Experiments in Fluids*, 63(7):118, 2022. ISSN 1432-1114. doi: 10.1007/s00348-022-03466-x.

J. H. Lee, Kevin, J. P. Monty, and N. Hutchins. Validating under-resolved turbulence intensities for PIV experiments in canonical wall-bounded turbulence. *Experiments in Fluids*, 57(8):129, Jul 2016. ISSN 1432-1114. doi: 10.1007/s00348-016-2209-6. URL `https://doi.org/10.1007/s00348-016-2209-6`.

S.-K. Lee, P. Manovski, and M. Jones. Assessing junction boundary layer and wake flow of a benchmark submarine model with tripped appendages. *Applied Ocean Research*, 149:104041, 2024. ISSN 0141-1187. doi: https://doi.org/10.1016/j.apor.2024.104041. URL `https://www.sciencedirect.com/science/article/pii/S0141118724001639`.

P. Manovski, M. Jones, S. Henbest, Y. Xue, M. Giacobello, and C. de Silva. Boundary layer measurements over a body of revolution using long-distance particle image velocimetry. *International Journal of Heat and Fluid Flow*, 83:108591, 2020. ISSN 0142-727X. doi: https://doi.org/10.1016/j.ijheatfluidflow.2020.108591.

P. Manovski, H. Ng, M. Giacobello, C. de Silva, W. Abu Rowin, N. Hutchins, and I. Marusic. Cross-validation of turbulent boundary layer measurements over an axisymmetric body of revolution. In *23rd Australasian Fluid Mechanics Conference, Sydney, Australia*, 2022.

J. W. Naughton and T. Liu. Photogrammetry in oil-film interferometry. *AIAA Journal*, 45(7):1620–1629, 2007. doi: doi.org/10.2514/1.24634. URL `doi.org/10.2514/1.24634`.

H. C. Ng, I. Marusic, J. P. Monty, N. Hutchins, and M. S. Chong. Oil film interferometry in high Reynolds number turbulent boundary layers. In *16th Australasian Fluid Mechanics Conference, Gold Coast, Australia*, 2007.

R. Örlü and R. Vinuesa. Instantaneous wall-shear-stress measurements: advances and application to near-wall extreme events. *Measurement Science and Technology*, 31(11):112001, aug 2020. doi: 10.1088/1361-6501/aba06f. URL `https://dx.doi.org/10.1088/1361-6501/aba06f`.

M. Samie, N. Hutchins, and I. Marusic. Revisiting end conduction effects in constant temperature hot-wire anemometry. *Experiments in Fluids*, 59(9):133, 2018. ISSN 1432-1114. doi: 10.1007/s00348-018-2587-z. URL `https://doi.org/10.1007/s00348-018-2587-z`.

J. A. Sillero, J. Jiménez, and R. D. Moser. One-point statistics for turbulent wall-bounded flows at Reynolds numbers up to $\delta^+ \approx 2000$. *Physics of Fluids*, 25(10):105102, 2013. doi: 10.1063/1.4823831.

C. Willert, M. Novara, D. Schanz, R. Geisler, M. Schroll, S. Ribergård, and A. Schröder. Multi-resolution, time-resolved PIV measurements of a decelerating turbulent boundary layer near separation. *14th International Symposium on Particle Image Velocimetry*, 1, 08 2021. doi: 10.18409/ispiv.v1i1.77.